Simulation of shrinkage-induced macrosegregation in a multicomponent alloy during reduced-gravity solidification

Ali Saad[1], Charles-André Gandin[2], Michel Bellet[2], Thomas Volkmann[3], Dieter Herlach[3]

[1]TRANSVALOR S.A., Parc de Haute Technologie, 06255 Mougins, France
[2]MINES ParisTech, Centre de Mise en Forme des Matériaux, UMR CNRS 7635, CS10207, 06904 Sophia Antipolis, France
[3]Institut für Materialphysik im Weltraum, Deutsches Zentrum für Luft- und Raumfahrt (DLR), 51147 Köln, Germany

Keywords: solidification, segregation, shrinkage, reduced-gravity, modeling

Abstract

Segregation is a key phenomenon responsible for altering alloys' properties during solidification. The factors that lead to solute partitioning at the scale of the solidified parts are related to movements of liquid and solid phases. However, when considering a reduced gravitational field, convection forces become less significant compared to other factors. Consequently, predicting segregation in this context requires considering other prevailing driving forces, namely solidification shrinkage that arises from the density difference between the liquid and solid phases. We propose a numerical model that accounts for energy conservation via a thermodynamic database, together with fluid momentum conservation and species conservation to predict segregation driven by solidification shrinkage in a multicomponent alloy. We apply it on a specific steel grade for which reduced-gravity experiments were performed via parabolic flights.

Introduction

Containerless solidification has drawn the attention of many researchers for over two decades [1] and is still an active research area. It allows reaching high degrees of undercooling, which was not possible in classical solidification setups. In the past, many simulations attempts [2, 3] were made to understand the hydrodynamics during electromagnetic levitation. However, these attempts considered only the liquid state, hence solidification and segregation were not simulated. In the current project, Chill Cooling for the ElectroMagnetic Levitator in Continuous Casting of steel (CCEMLCC), we aim at studying the effect of directional solidification triggered by a chill contact. In this European Space Agency (ESA) project, we are mainly interested in the formation of reduced-gravity flow by density differences between the liquid phase and the solid phases, created during solidification and the subsequent effects on the segregation behaviour in a steel droplet. The objective is then providing a test case for numerical simulation.

Numerical model

Interface tracking

The level set method [4] is employed in the current work to capture the dynamic interface separating the liquid metal and the argon gas. Its advantage lies in the way the interface

between two domains, F_1 and F_2 is implicitly captured, unlike other methods where the exact interface position is needed. By taking $d_\Gamma(\boldsymbol{x})$ as the minimum distance separating a point x from an interface Γ, we can define the distance function, denoted α, as: $\alpha = d_\Gamma(\boldsymbol{x})$ if the point belongs to F_1, $\alpha = -d_\Gamma(\boldsymbol{x})$ if the point belongs to F_2, and $\alpha = 0$ if the point belongs to the interface Γ. The definition of a signed distance function leads to the smoothed Heaviside function, denoted H. The latter gives the presence of one domain with respect to the interface position. It is given by:

$$H = \begin{cases} 0 & \text{if } \alpha(\boldsymbol{x}) < -\varepsilon \\ 1 & \text{if } \alpha(\boldsymbol{x}) > \varepsilon \\ \frac{1}{2}\left(1 + \frac{\alpha(\boldsymbol{x})}{\varepsilon} + \frac{1}{\pi}\sin\left(\frac{\pi\alpha(\boldsymbol{x})}{\varepsilon}\right)\right) & \text{if } -\varepsilon \leq \alpha(\boldsymbol{x}) \leq \varepsilon \end{cases} \tag{1}$$

where the interval $[-\varepsilon; +\varepsilon]$ is an artificial interface thickness around the zero distance. Eq. (1) is used to perform an *arithmetic mixing* of the variables. Therefore, a physical quantity $\langle\psi\rangle$ is mixed between by: $\widehat{\langle\psi\rangle} = H^M \langle\psi^M\rangle + H^A \langle\psi^A\rangle$, where capital superscripts M and A respectively refer to metal and argon domains. Within each domain, the properties are averaged among phases by considering a representative volume element, hence no direct interface tracking between the phases. For instance, a metal-related property is averaged using: $\langle\psi^M\rangle = \sum_{\phi\in M} g^\phi \langle\psi\rangle^\phi$, where ϕ is a phase referring to liquid (l) or solids (s) in the metal, while in the argon domain, the only phase is the argon gas (a) itself, so that $g^a = 1$, resulting in the equality $\langle\psi^A\rangle = \langle\psi\rangle^a$.

Monolithic conservation equations

The monolithic model combines all conservation equations derived for metal and gas in a unique set of equations, to be solved on a fixed Eulerian mesh by the finite element method. The model couples averaged conservation equation for mass, liquid momentum, energy and chemical species, in a weak fashion.

Mass and momentum conservation An arithmetic mixing between the molten metal's average velocity, $\langle\boldsymbol{v^l}\rangle$, and the argon's average velocity, $\langle\boldsymbol{v^a}\rangle$, gives the system's fluid velocity, $\langle\boldsymbol{v^F}\rangle$. The metal domain thus consists of a single fluid phase, i.e. the liquid plus the solid phases. We further assume that the latter phase forms in fixed and rigid structures, $\boldsymbol{v^s} = 0$ (assuming that solidification results in an undeformable columnar dendritic, peritectic and eutectic structures, without any freely moving equiaxed dendritic structure), while the domain surrounding the metal entirely consists of argon gas. Finally, the monolithic mass balance writes:

$$\boldsymbol{\nabla}\cdot\langle\boldsymbol{v^F}\rangle = H^M\left(-\frac{1}{\langle\rho\rangle^l}\left(\frac{\partial\langle\rho\rangle^M}{\partial t} + \langle\boldsymbol{v^l}\rangle\cdot\boldsymbol{\nabla}\langle\rho\rangle^l\right)\right) \tag{2}$$

The momentum balance is transformed into averaged Navier-Stokes-Darcy equations as follows:

$$\begin{cases} \widehat{\rho}\left(\dfrac{\partial\left\langle \boldsymbol{v}^{\boldsymbol{F}}\right\rangle}{\partial t}+\dfrac{1}{g^{F}}\boldsymbol{\nabla}\cdot\left(\left\langle \boldsymbol{v}^{\boldsymbol{F}}\right\rangle\times\left\langle \boldsymbol{v}^{\boldsymbol{F}}\right\rangle\right)\right)= \\ -g^{F}\boldsymbol{\nabla}p-2\widehat{\mu}\boldsymbol{\nabla}\cdot\left(\overline{\overline{\boldsymbol{\nabla}}}\left\langle \boldsymbol{v}^{\boldsymbol{F}}\right\rangle+\overline{\overline{\boldsymbol{\nabla}^{\mathrm{t}}}}\left\langle \boldsymbol{v}^{\boldsymbol{F}}\right\rangle\right)-g^{F}\widehat{\mu}\widetilde{\mathbb{K}}^{-1}\left\langle \boldsymbol{v}^{\boldsymbol{F}}\right\rangle+\widehat{\rho g}\mathbf{g} \\ \\ \boldsymbol{\nabla}\cdot\left\langle \boldsymbol{v}^{\boldsymbol{F}}\right\rangle=H^{M}\left(-\dfrac{1}{\left\langle \rho\right\rangle^{l}}\left(\dfrac{\partial\left\langle \rho\right\rangle^{M}}{\partial t}+\left\langle \boldsymbol{v}^{\boldsymbol{l}}\right\rangle\cdot\boldsymbol{\nabla}\left\langle \rho\right\rangle^{l}\right)\right) \end{cases} \tag{3}$$

The mechanical properties used in eq. (3) are mixed as follows:

$$\text{Fluid fraction}: g^{F}=H^{M}g^{l}+H^{A}g^{a}=H^{M}g^{l}+H^{A} \tag{4}$$

$$\text{Density}: \widehat{\rho}=H^{M}\left\langle \rho\right\rangle^{l}+H^{A}\left\langle \rho\right\rangle^{a} \tag{5}$$

$$\text{Dynamic viscosity}: \widehat{\mu}=H^{M}\mu^{l}+H^{A}\mu^{a} \tag{6}$$

$$\text{Weight force}: \widehat{\rho g}\mathbf{g}=H^{M}g^{l}\left\langle \rho\right\rangle^{l}\mathbf{g}+H^{A}g^{a}\left\langle \rho\right\rangle^{a}\mathbf{g}=H^{M}g^{l}\left\langle \rho\right\rangle^{l}\mathbf{g}+H^{A}\left\langle \rho\right\rangle^{a}\mathbf{g} \tag{7}$$

The Darcy term depends on the fluid fraction, g^{F}, and the secondary dendrite arm spacing, λ_{2}, through a modified permeability model:

$$\widetilde{\mathbb{K}}=\frac{\lambda_{2}^{2}{g^{F}}^{3}}{180\left(1-g^{F}\right)^{2}} \tag{8}$$

As for the weight force in both domains, it is taken into account via eq. (7). The phase densities may vary as functions of other parameters such as temperature or phase composition, creating buoyancy forces inside the fluid. In our approach, $\left\langle \rho\right\rangle^{l}$ is a tabulated function of temperature and phase intrinsic composition (w_{i}^{l} is the liquid composition of the i^{th} species), given by a suitable thermodynamic database [5, 6]. We keep however the argon phase density $\left\langle \rho\right\rangle^{a}$ constant, so as to prevent a mixture of convection forces around the interface between domains, which helps stabilise the fluid flow resolution.

Energy conservation We model the heat transfer and the phase change using a temperature-based resolution [7] The method relies on predefined thermodynamic mappings [5] computed at full equilibium. The gouverning equation is given by:

$$\frac{\partial\widehat{\left\langle \rho h\right\rangle}}{\partial t}+\left\langle \boldsymbol{v}^{\boldsymbol{F}}\right\rangle\cdot\boldsymbol{\nabla}\widehat{\left(\rho h\right)^{F}}=\boldsymbol{\nabla}\cdot\left(\widehat{\left\langle \kappa\right\rangle}\boldsymbol{\nabla}T\right)+\widehat{\Phi} \tag{9}$$

The solution of eq. (9) is $\widehat{\left\langle \rho h\right\rangle}$, a mixed field between both domains average volumetric enthalpies. The other parameters are $\widehat{\left(\rho h\right)^{F}}$ and $\widehat{\left\langle \kappa\right\rangle}$ which denote respectively the fluids' mixture volume enthalpy and the mixture of average thermal conductivities. The last term, $\widehat{\Phi}$, is an average heat source accounting for energy change caused by the alloy's shrinking volume [8]. As no volume change was considered for the argon, $\widehat{\Phi}$ is present only in the metal's energy balance.

Species conservation The conservation of species mass is gouverned by the following equation using the macroscopic solute diffusion coefficient in the liquid, D^l:

$$\begin{aligned}
&\langle\rho\rangle^M \frac{\partial\widehat{\langle w\rangle}}{\partial t} + \langle\rho\rangle^l \langle \boldsymbol{v^l}\rangle \cdot \boldsymbol{\nabla}\widehat{\langle w\rangle} - \boldsymbol{\nabla}\cdot\left(g^l \langle\rho\rangle^l D^l \boldsymbol{\nabla}\widehat{\langle w\rangle}\right) = \\
&- \frac{\partial \langle\rho\rangle^M}{\partial t}\left[\left(\langle w\rangle^M\right)^t - \left(\langle w\rangle^l\right)^t\right] \\
&+ \langle\rho\rangle^l \langle \boldsymbol{v^l}\rangle \cdot \boldsymbol{\nabla}\left(\left(\langle w\rangle^M\right)^t - \left(\langle w\rangle^l\right)^t\right) - \boldsymbol{\nabla}\cdot\left[g^l \langle\rho\rangle^l D^l \boldsymbol{\nabla}\left(\left(\langle w\rangle^M\right)^t - \left(\langle w\rangle^l\right)^t\right)\right]
\end{aligned} \tag{10}$$

The right-hand side terms emerge from a variable splitting.

Computational configuration

Geometry and boundary conditions

The simulation considers only 1/4 of the droplet-gas system, given the axial symmetry of the problem. The steel sample is not perfectly spherical initially as surface oscillations perturb the equilibrium shape. The droplet is hence an ellipsoid having a vertical minor axis of 5.68 mm and a horizontal major axis of 6.6 mm, as shown in fig. 1. The bottom is a planar surface (diameter of 2 mm, where the contact is initiated). Also in fig. 1, the alloy is immersed in a gas medium (argon), such that both subdomains form together 1/4 of a cylinder having 8 mm in radius and 8 mm in height. The mesh is automatically adapted to the moving interface using anisotropic elements to reduce the computational cost while maintaining sufficient numerical accuracy. The time step is 0.01 s. For the velocity-pressure boundary conditions, fig. 2 shows the no-slip condition imposed on the droplet-substrate surface, since this area solidifies in the first place without further fluid motion. The only thermal boundary condition is a convection flux with constant heat transfer coefficient, h_{ext} ($6 \times 10^4\,\text{W}\,\text{m}^{-2}\,\text{K}^{-1}$), and constant external temperature, T_{ext} (25 °C), that replaces the ceramic chill. We consider that the heat flux dissipated by the chill is dominant with respect to other heat transfer mechanisms (e.g. radiation). The gravitational acceleration magnitude is assumed to be in order of $5 \times 10^{-5}\,\text{m}\,\text{s}^{-2}$, hence designated by $\mu\mathbf{g}$, as typically measured in under reduced-gravity conditions.

Choice of alloy

Various steel grades were considered in the CCEMLCC project. Each grade was assigned to a specific experiment. We limit our study to the steel assigned for TEXUS sounding rocket missions, the grade is designated as "*b1*" alloy. Its nominal composition is given in table 1. The current approach relies on thermodynamic tabulations to determine density and composition for all phases as functions of the evolving average alloy composition. By considering three solute species, a quaternary Fe-C-Si-Mn alloy referred to as *b1Quat* alloy, is used to predict segregation.

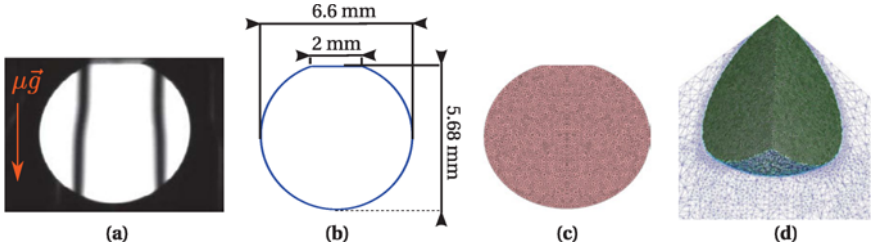

Figure 1 – The camera frame (a) before the onset of solidification gives the essential information [9] to (b) rebuild the 2D droplet geometry then (c) a standalone 2D mesh used to obtain (d) the final immersed axisymmetrical 3D mesh, including the argon reservoir surrouding the droplet.

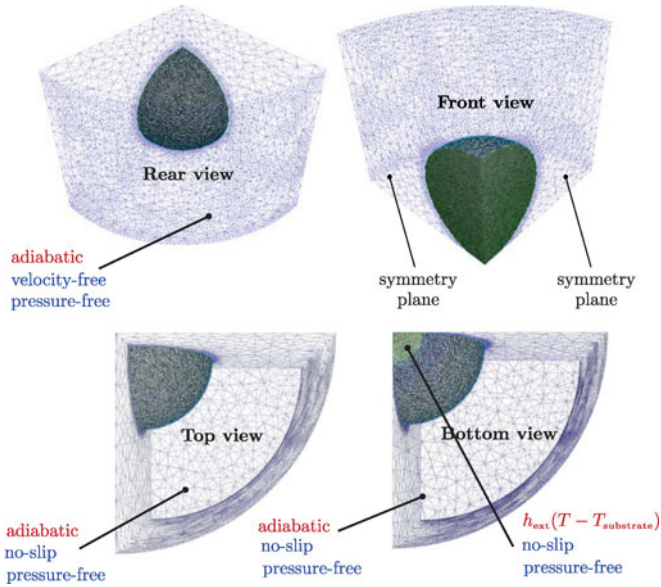

Figure 2 – 3D views showing the thermal (red) and mechanical (blue) boundary conditions used in reduced-gravity simulations.

Table 1 – Nominal composition (wt.%) of the experimental *b1* steel and its simulation quaternary equivalent alloy, *b1Quat*.

Alloy	C	Si	Mn	Al	S	P
b1	0.105	0.268	0.636	0.0067	0.009	0.0189
b1Quat	0.105	0.268	0.636	-	-	-

Results and discussion

Shrinkage-induced flow

The flow pattern shown in fig. 3 reveals distinct regions at 0.25 s and 1 s: upward flow driven by solidification shrinkage contributes to a slight enrichment by inverse segregation, while a downward flow driven by gravity, redistributes species in the containerless melt. At 8 sec, the mushy zone reaches the droplet vertex marking a flow pattern change. Upon completely solidifying, the droplet forms a rigid and static solid, surrounded by natural argon flow, seen at 20 s in fig. 3.

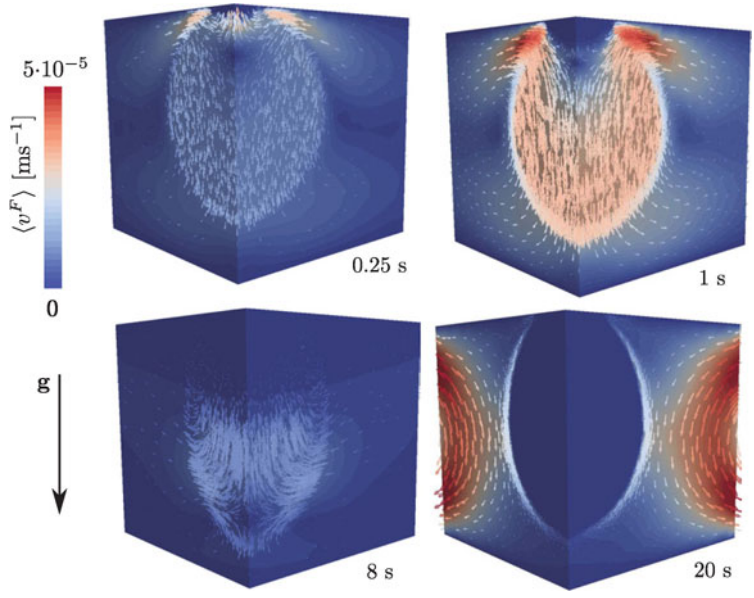

Figure 3 – Flow patterns in reduced-gravity solidification with shrinkage.

Segregation

The shrinkage-induced fluid flow is behind the reduced-gravity segregation shown at different stages in fig. 4. A restricted region of positive segregation settles at the contact area with the substrate, from the first second after the contact. Later, between 2 s and 8 s, the solid front advances in the melt, creating a noticeable negatively segregated area, about 4% less than the nominal composition, just below the positive segregation zone. This is not the expected inverse segregation profile obtained by directional solidification. Usually, we would expect that the composition decreases gradually once the solid front advances in time. To interpret this unusual observation, we refer to the fluid flow shown earlier in fig. 3. At 0.25 s, a no-velocity isovolume (i.e. depicting a volume with null velocity magnitude) forms between the two distinct regions of upward and downward flow.

The strong negative divergence that settles in this area results in solute depletion in the two directions and due to the various driving forces. However, at 1 s, the no-velocity isovolume clearly shrinks in a matter of only 0.75 s. That is because the initial temperature gradient is the highest during the process, then it decreases gradually. Since a higher temperature gradient produces a greater cooling flux according to the Fourier model, solidification is faster in the beginning and the volume shrinkage is greater, hence the shrinkage flow coexists with the gravity flow. As the transformation progresses, shrinkage flow becomes insignificant compared to the latter, therefore the negative segregation intensity decreases gradually from 2.2 mm to 4.3 mm from the chill, corresponding to the first seconds of contact. This result is also shown in fig. 5 for carbon, where we plot the relative segregation profile along the vertical rotation axis of the droplet. At 8 s, fig. 3 shows the zero-velocity isovolume moved down the vertical revolution axis by following the solidification front, then vanishing at about 10 s. It means that from this point in time, the flow is dissipated by the mushy zone's low permeability, hence the low-magnitude shrinkage flow dominates again.

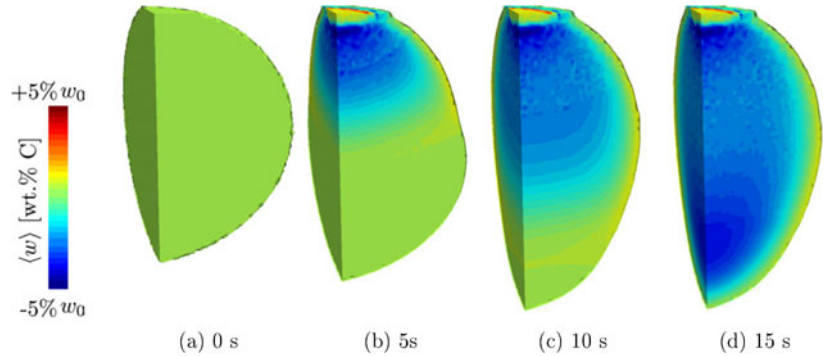

Figure 4 – Evolution of the carbon average composition with solidification time, showing evidence of mesosegregation and shape deformation between 0 s and 15 s.

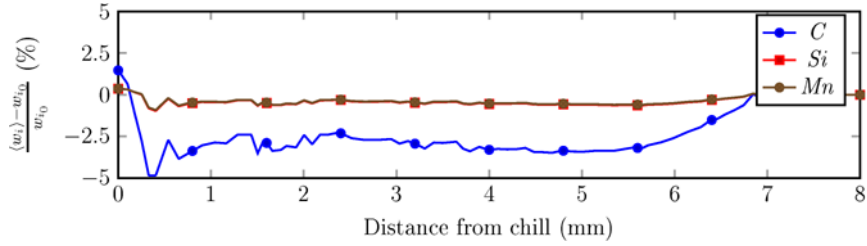

Figure 5 – Relative segregation profiles for each chemical species as function of the distance from the chill, plotted along the vertical revolution axis of the solidified sample.

Conclusion

A multicomponent alloy solidification has been studied in a reduced-gravity environment. Segregation due to shrinkage-feeding flow and gravitational flow is studied for each chemical species, carbon, silicon and manganese. The simulation results show a flow competition in reduced-gravity solidification, which affects the final solidified shape, and the segregation intensity.

Acknowledgments

This work was conducted as a part of the Microgravity Applications Promotion (MAP) program, funded by the European Space Agency - ESTEC (Noordwijk, NL) under the CCEMLCC project (grant AO-2004-017).

References

[1] R. Willnecker, D. M. Herlach, and B. Feuerbacher. "Containerless undercooling of bulk Fe-Ni melts". *Applied Physics Letters* 49 (20) (11/1986), pp. 1339–1341.

[2] J. Lee et al. "Magnetohydrodynamic Modeling and Experimental Validation of Convection Inside Electromagnetically Levitated Co-Cu Droplets". *Metallurgical and Materials Transactions B* 45 (3) (12/2013), pp. 1018–1023.

[3] J. Lee, X. Xiao, D. M. Matson, and R. W. Hyers. "Numerical Prediction of the Accessible Convection Range for an Electromagnetically Levitated Fe50Co50 Droplet in Space". *Metallurgical and Materials Transactions B* 46 (1) (09/2014), pp. 199–207.

[4] S. Osher and J. A. Sethian. "Fronts propagating with curvature-dependent speed: Algorithms based on Hamilton-Jacobi formulations". *Journal of Computational Physics* 79 (1) (11/1988), pp. 12–49.

[5] J.-O. Andersson, T. Helander, L. Höglund, P. Shi, and B. Sundman. "Thermo-Calc & DICTRA, computational tools for materials science". *Calphad* 26 (2) (06/2002), pp. 273–312.

[6] TCFE6. *TCFE6: a thermodynamic database for different kinds of steels and Fe-based alloys.* Stockholm, SE, 2010.

[7] A. Saad, C.-A. Gandin, and M. Bellet. "Temperature-based energy solver coupled with tabulated thermodynamic properties – Application to the prediction of macrosegregation in multicomponent alloys". *Computational Materials Science* 99 (03/2015), pp. 221–231.

[8] A. Saad. "Numerical modelling of macrosegregation formed during solidification with shrinkage using a level set approach". PhD Thesis. MINES ParisTech, 2016.

[9] C.-A. Gandin. *Project ESA-MAP CCEMLCC phase #2 – Final Report.* 2014.